A 10.1-ENOB, 6.2-fJ/conv.-step, 500-MS/s, Ringamp-Based Pipelined-SAR ADC With Background Calibration and Dynamic Reference Regulation in 16-nm CMOS

Jorge Lagos, *Senior Member, IEEE*, Nereo Markulić, *Member, IEEE*, Benjamin Hershberg, *Member, IEEE*, Davide Dermit, *Member, IEEE*, Mithlesh Shrivas, *Member, IEEE*, Ewout Martens, *Member, IEEE*, and Jan Craninckx, *Fellow, IEEE*

Abstract—This work presents a single-channel, fully dynamic pipelined-SAR ADC with relaxed architectural tradeoffs thanks to the use of ring amplification and background calibration. It leverages a novel SAR quantizer and narrowband dither injection to achieve fast and comprehensive background calibration of DAC mismatch, interstage gain, and ring amplifier (ringamp) linearity and bias optimality. The ADC also includes an on-chip, wide-range, fully dynamic reference regulation system. Implemented in 16-nm CMOS, it consumes 3.3 mW at 500 MS/s (including regulation) and achieves 10.1 ENOB and 75.5-dB SFDR, resulting in Schreier and Walden figure-of-merit (FoM) values of 171.1 dB and 6.2 fJ/conv.-step, respectively.

Index Terms—A/D, ADC, asynchronous, background calibration, dither, fully dynamic, low-power, narrowband dither, pipelined SAR, reference buffer, reference regulation, ringamp, ring amplification, ring amplifier, SAR quantizer, single-channel.

I. Introduction

THE pipelined SAR ADC is a well-established architecture for applications requiring medium-to-large resolutions and bandwidths in the hundreds-of-MHz range, as it combines the good power efficiency and scalability of SAR conversion with the speed benefits of pipelined converters [1].

In this architecture, the topology choices for both the SAR quantizers and the residue amplifiers play a determinant role in the achievable speed, linearity, and power efficiency, with well-defined tradeoffs. On the quantizer side, solutions like the multi-comparator quantizer [2]–[4] and multi-bit-per-cycle conversion [5]–[7] can increase speed in exchange
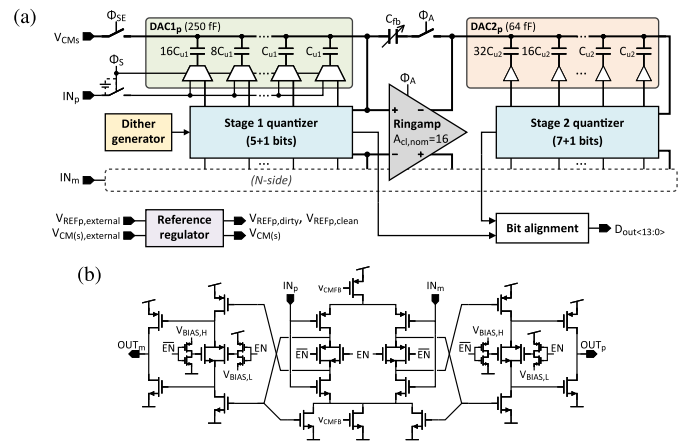
Fig. 1. (a) Proposed ADC architecture and (b) ringamp implementation [16].

for calibration and/or implementation complexity. On the residue amplifier side, the use of open-loop amplification [3], [8]–[10] has also been demonstrated as an effective means for enhancing speed and power efficiency, often at the cost of greater calibration complexity [10]–[12].

Ring amplification [13] is an alternative closed-loop amplification paradigm, and in recent years has broadly advanced the state-of-the-art in power efficiency for both pipelined [14]–[16] and pipelined-SAR ADCs [17]–[20]. Whereas recent ringamp-based pipelined ADCs rank at the forefront of the per-channel speed boundary, all previously reported ringamp-based pipelined SARs operate at speeds below the upper bound established by open-loop-amplifier-based designs [1]. This is to a large extent the result of two factors: target applications with high ENOB targets which in general lead to slower speeds regardless of the amplifier used, and a calibration-free approach where PVT robustness was ensured through extra design margin, at the expense of speed.

In this work, we present a pipelined-SAR ADC (see Fig. 1) that exploits ring amplification and background calibration to simultaneously achieve high speed and power efficiency [21]. Compared to open-loop-amplifier-based pipelined SARs, a ringamp helps to relax several key architectural

tradeoffs. First, due to their closed-loop nature, ringamps are unconstrained in terms of the residue amplitude size they can process at their input. As a result, both the LSB size in the front-end stage (Stage 1) and the ADC full-scale can be of any size. This allows for a relatively small number of bits to be quantized by the Stage-1 SAR, minimizing the critical Stage-1 conversion time and maximizing the error tolerance provided by, e.g., 1 LSB of interstage redundancy, due to a larger LSB size. Second, ringamps can process nearly rail-to-rail output swings while maintaining high linearity. As a result, the LSB size in the back-end stage (Stage 2) can also be maximized due to a large interstage gain factor, thus relaxing the noise, error, and metastability requirements in this stage and allowing the use of a fast, power-efficient quantizer.

Several background calibration loops are used in the proposed architecture to correct errors, ensure robustness, optimize performance, and maximize power efficiency. First-order interstage-gain calibration corrects for finite-gain error (higher-order components of gain error do not require correction due to the highly-linear output characteristic of the ringamp [22]). DAC mismatch calibration is used in Stage 1 to allow for a minimum-area DAC sized only for thermal noise requirements. Finally, a novel approach is introduced for optimizing the ringamp biasing and settling behavior in the background to guarantee robust PVT operation. All these calibration techniques are implemented using narrowband dither injection at the Stage-1 quantizer, leveraging a new SAR quantizer developed to support this capability.

The core pipeline in this work exploits fully-asynchronous, event-based operation [23] to achieve fully-dynamic power consumption. In order to extend this desirable property to the overall ADC, we also introduce a fully-dynamic reference buffer based on Split-Reference Regulation [15]. Especially tailored for pipelined-SAR operation, the regulator improves upon the implementation in [15] by using charge-pumping to synthesize a wider range of reference voltages, with increased power efficiency and lower area requirements.

This article is organized as follows. Section II discusses the SAR quantizer introduced in this work. Section III presents the details of the proposed narrowband-dither injection technique and the background calibration loops that utilize it. The fully-dynamic on-chip reference regulator is described in Section IV. Experimental results are reported in Section V. Finally, Section VI summarizes the conclusions of this work.

II. MULTI-LATCH SAR QUANTIZER

A. Review of Traditional SAR Quantizer Topologies

SAR quantizers suffer from an intrinsic speed-resolution tradeoff due to the serial nature of their operation. This sets an upper limit on their achievable speed, and as a result topologies with minimal critical-path decision delay are essential when high resolution and conversion speed are required.

Moreover, in pipelined and pipelined-SAR ADCs the ability to inject a pseudorandom noise (PN) dither signal into the analog path is often desired, as it enables the background calibration of several analog non-idealities, including DAC mismatch and interstage gain [24]. PN modulation of the
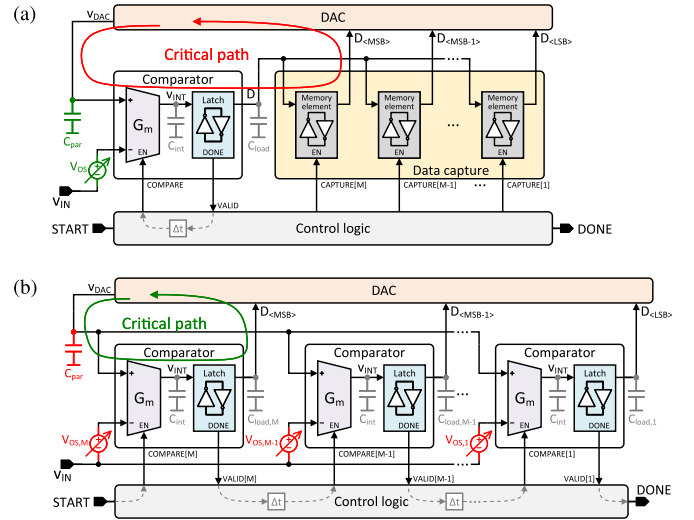

Fig. 2. Traditional SAR quantizer topologies. (a) Single-comparator. (b) Multi-comparator ("loop-unrolled").

comparison threshold(s) of a stage sub-ADC is a particularly attractive way to inject dither because it does not rely on analog matching [24]. As such, a SAR quantizer able to easily vary its comparison thresholds on-the-fly with no performance loss is highly desirable [25], [26].

Existing single-bit-per-cycle SAR quantizers can be broadly classified into single-comparator and multi-comparator implementations, according to the number of comparators used. These architectures are now reviewed in terms of critical-path length, number of comparator offsets needed to calibrate, and amenability for dither injection.

1) Single-Comparator SAR Quantizer: Fig. 2(a) shows the structure of a single-comparator SAR quantizer [27]–[29]. As the name implies, it is implemented using a single comparator whose decisions are sequentially captured by several memory elements, one for each of the M bits resolved. The commonly-used comparator structure in [30], shown here, is composed of a memory-less preamplifier G_m followed by a regenerative latch. The preamplifier converts the input voltage into a current that is integrated on a capacitance C_{int} (usually a non-explicit, parasitic capacitor) and the resulting voltage v_{INT} is applied to the regenerative latch to produce the digital comparison result. Once the comparator resolves a bit (VALID signal is asserted) and its output is captured, it goes into reset, which usually happens within the time allocated for DAC settling, whose duration is set by ensuring an adequate delay Δt between the assertion of VALID and the launching of the next comparison.

Due to its use of a single comparator, this topology benefits from simple offset calibration, small input capacitance (C_{par}) and minimal area. However, it suffers from long critical-path length due to the memory elements required for data capture, which also increase the comparator load (C_{load}). Also, although it is possible to perform dither injection in this topology, existing methods usually increase the capacitive loading at critical internal nodes (e.g., C_{int}) [31], thus penalizing speed.
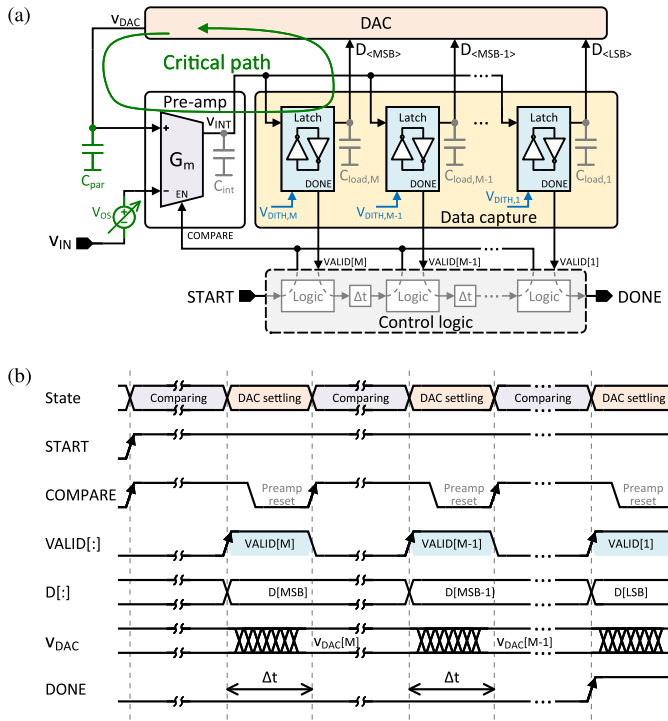
Fig. 3.   (a) Proposed multi-latch SAR quantizer and (b) its timing diagram.

Fig. 4.   Detailed implementation of the proposed quantizer.

2) Multi-Comparator SAR Quantizer: The multi-comparator quantizer shown in Fig. 2(b) is an attempt to improve upon the classical single-comparator approach in several ways. Originally proposed in [2] under the name of "comparator-based SAR controller," it is better known as the "loop-unrolled" SAR. In this architecture a dedicated comparator is used for each bit resolved, thereby eliminating the need for explicit data capture logic. Instead, the regenerative-latch output of each comparator is hardwired directly to a corresponding DAC control input. The control logic is also greatly simplified in this architecture and can be as simple as the Δt delays required to ensure adequate DAC settling. Finally, the use of dedicated comparators also enables the possibility of implementing per-bit dither injection in this architecture.

Due to its minimal critical-path length, this topology achieves the fastest conversion speed. However, it suffers from complex offset calibration (as all the individual offsets $V_{OS,i}$ need to be compensated) and large input capacitance and area.

B. Proposed Multi-Latch SAR Quantizer

Fig. 3 shows the proposed quantizer along with a simplified timing diagram. Conceptually lying halfway between single- and multiple-comparator approaches, it is composed of a single preamplifier that sequentially drives multiple latches. Like in the multi-comparator quantizer, these latches serve as the data capture register and interface to the DAC directly without the need for additional memory elements.

This multi-latch architecture retains the low calibration complexity benefit of the single-comparator topology, because the shared preamplifier dominates the input-referred offset due
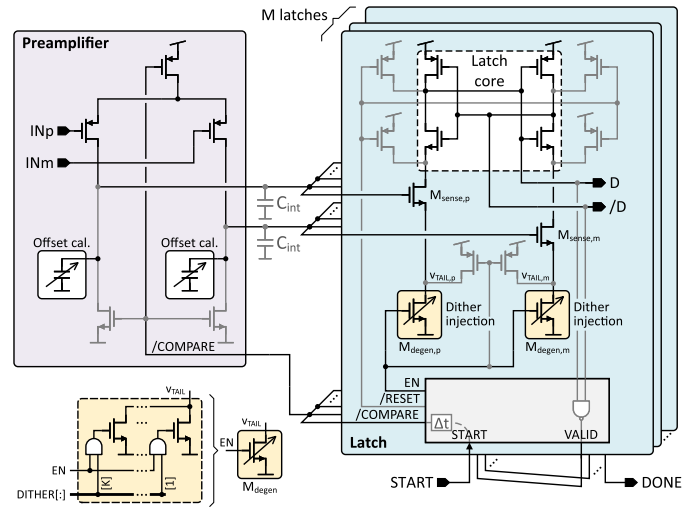
to random mismatch. It also inherits the speed benefits of the loop-unrolled topology due to the direct connection of latch outputs to DAC inputs, while avoiding its drawbacks of increased offset calibration complexity and large input capacitance. In addition, like the multi-comparator quantizer, the multi-latch quantizer is capable of variable-amplitude, per-bit dither injection, which can be accomplished by embedding offset voltages $V_{DITH,i}$ in the individual latches.

The defining features of the proposed architecture also introduce some practical implementation challenges. Due to its multiplexed use, the preamplifier should ideally be able to reset in the time Δt budgeted for DAC settling, as illustrated in Fig. 3(b). Also, in this topology the preamplifier load increases with the number of resolved bits. This, however, can be of no concern if the number of bits is kept low or if the preamplifier load needs to be high anyway due to noise constraints [32].

The implementation of the proposed quantizer is detailed in Fig. 4. The dynamic preamplifier and the regenerative latches are similar to the ones in [33], with appropriate modifications. The control logic block in each latch includes a tri-state-output buffer for driving the /COMPARE control line. The latches thus take turns sequentially to connect to this line in order to fire and reset the preamplifier for each comparison. Also, capacitive DACs are added at the preamplifier outputs to compensate for its offset.

In the latches, tail devices $M_{degen,(p,m)}$ and local control logic are added to allow the selective enabling or disabling of the core latch by means of the control signals EN and /RESET. Their operation is as follows. When a given latch is active, both its EN and /RESET signals are high and its tail nodes $v_{TAIL,(p,m)}$ see a low impedance to ground, allowing the sensing devices $M_{sense,(p,m)}$ to sense the preamplifier output polarity and transfer it to the latch core. Conversely, when a latch is inactive its EN and /RESET signals are low so that its tail nodes are pulled-up to the positive supply along with all the latch-core nodes, thereby shutting down the sensing devices and effectively disconnecting the latch from the preamplifier. Once a latch resolves a bit, its VALID signal is fed to
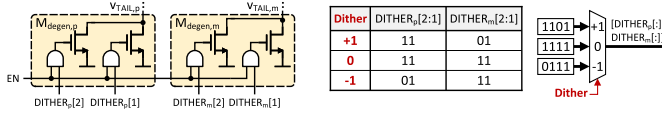
Fig. 5. Example of dither injection in a latch using source-degeneration arrays with $K = 2$ devices per side.

the subsequent latch and used to fire the next comparison after a delay Δt allocated for DAC settling. The latches retain their decisions until the full quantizer is reset.

As depicted in Fig. 4, the per-bit dither injection is accomplished by implementing the latch tail devices $M_{\text{degen},(p,m)}$ as programmable source-degenerating arrays, each composed of K NMOS transistors that can be independently enabled according to the value of the DITHER[:] codeword. Thus, offset voltages can be introduced by using different DITHER[:] values on each half of the latch, effectively shifting the comparison threshold by a corresponding $V_{\text{DITH},i}$ amount. As an example, Fig. 5 shows a minimalistic implementation with $K = 2$, illustrating how the three-level logic dither values can be translated into suitable codewords via a MUX whose output controls how many source-degenerating devices are enabled on each latch side. The implementation of Fig. 4 has the benefit of supporting variable-amplitude dither injection natively, as the magnitude of the introduced offset can be made variable by having $K \geq 2$ unary devices or by using non-unary devices. The dither codewords DITHER[:] are programmed into the latch before the quantizer begins operating (during input signal tracking), which significantly relaxes the speed requirements and the power spent for dither injection in comparison to a single-comparator architecture.

In this work, the frontend quantizer is sized for speed, achieving a 1-mV-input resolution time of 90 ps, an input-referred noise of 1 mV$_{\text{rms}}$, and consuming 140 fJ/bit. Its input capacitance is 3 fF and the residual offset after calibration is <5 mV$_{\text{rms}}$, which together with the injected dither (5 mV nominal) is absorbed by the interstage redundancy. The preamplifier load C_{int} is 4.8 fF, composed of 3.4 fF from the input capacitance of the six latches and 1.4 fF from routing parasitics.

III. BACKGROUND CALIBRATION

Stage-1 DAC mismatch and interstage gain are digitally corrected in this design, leveraging on-chip, noninvasive, narrowband-dither calibration mechanisms that operate in the background during normal ADC operation. In this section, we discuss the principles and implementation aspects of these techniques. Moreover, we show how the injected dither is also leveraged for linearity and bias optimization of the residue amplifier, ensuring robust, PVT-resilient operation.

A. Traditional Broadband-Dither-Based Calibration

We start by conceptualizing the general dither-based background calibration principle, considering its application to interstage-gain correction. Let us assume the canonical two-stage pipelined architecture shown in Fig. 6(a) where
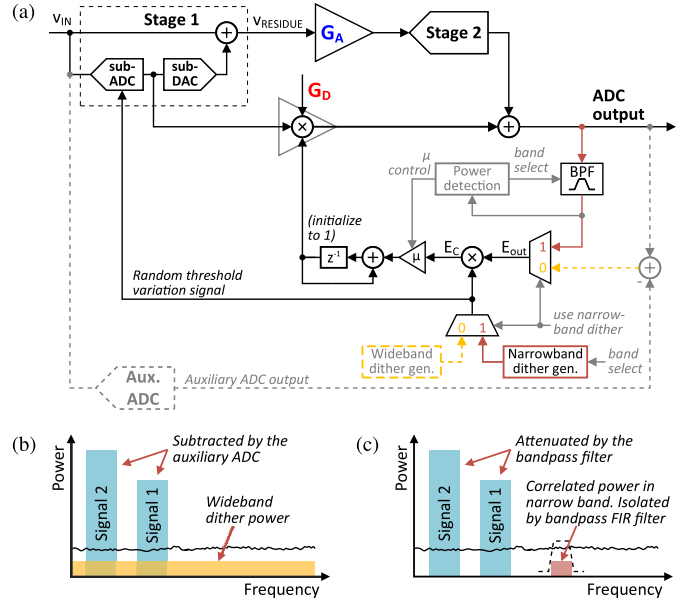

Fig. 6. (a) Conceptual dither-based interstage-gain calibration and associated spectra considering (b) wideband and (c) narrowband dither injection.

the sub-ADC within the first stage contains a programmable input-referred offset that can be updated from cycle to cycle. Moreover, let us assume that the interstage amplification G_A has 1-bit redundancy, such that under ideal operating conditions the amplified residue never exceeds half of the Stage-2 quantization range. When a PN dither sequence is used to modulate the sub-ADC offset, a proportional increase in quantization noise will appear in the analog output residue of Stage 1. However, thanks to redundancy, the error is fully corrected during the digital output reconstruction [24], and as long as the residue v_{RESIDUE} (after amplification by G_A) falls within the linear quantization range of Stage 2, the impact of the "error" induced by the sub-ADC offset variation is nulled. However, for accurate (corrective) reconstruction, it is imperative that the analog interstage gain G_A is known, i.e., that the digital reconstruction gain G_D matches G_A to sufficient accuracy. Under these conditions, the overall ADC digital output remains unaffected by the injected dither, accurately representing the quantized input signal v_{IN}. In contrast, when $G_A \neq G_D$ the ADC output becomes corrupted. It inaccurately represents v_{IN}, and carries some non-zero power correlated with the injected dither. This dither-correlated energy can be tracked and minimized in the background by appropriate readjustment of G_D, and an LMS-based correction loop [see Fig. 6(a)] can be built in the digital domain to achieve this, as described below.

For the sake of explanation, let us initially assume that the injected dither is wideband, as depicted by the spectrum in Fig. 6(b) [and flag use narrowband dither = "0" in Fig. 6(a)]. Moreover, let us assume there exists an ideal auxiliary ADC which converts the same input signal v_{IN} as the main ADC, but without the presence of dither [see Fig. 6(a)]. The dither-correlated energy at the main ADC output can then be reliably tracked, as v_{IN} can be easily removed from the

main ADC output by subtracting the auxiliary ADC output to produce a difference E_{OUT} that holds information pertaining only to errors induced within the main ADC. To estimate the dither-correlated energy, E_{OUT} is multiplied with the injected dither sequence, obtaining a product E_C that will have a positive or negative dc component depending on whether G_A is larger or smaller than G_D, respectively. This signal is then digitally integrated (with an integration gain determined by a constant μ), and the output of the integrator is used to scale the digital reconstruction gain G_D. The integrator will then gradually drift toward an optimum value that ensures $G_D = G_A$. Under this condition the reconstruction is again accurate, E_C becomes a zero-mean signal, and the integrator output varies only slightly around its optimum value due to the presence of other noise and error sources in the main ADC output that the auxiliary ADC does not cancel. Notably, the convergence speed of this algorithm is proportional to the integration constant μ but the variation around the final estimate (i.e., noise in the estimation) is inversely proportional to it. In other words, the integration constant μ trades off convergence speed for estimation noise.

Obviously, an ideal auxiliary ADC does not exist in practice, so the input signal cannot be subtracted from the ADC output before correlation with the dither sequence. Alternatively, the algorithm can also operate without the removal of v_{IN}, but then the small dither-correlated power present in E_{OUT} is swamped by the much larger signal power now also present in E_{OUT}, which injects a large amount of noise into E_C. To circumvent this, the integration constant μ needs to be extremely small, and although this filters out the estimation noise, it also slows down the estimation process, rendering the algorithm impractical for real-time PVT tracking.

To address the problem of limited estimation speed and accuracy, [24] makes use of a split-ADC architecture where two parallel, half-sized main ADC paths operate with the same input signal but with independent dither. Although the signal components can then be successfully removed from the ADC output to isolate the dither information, this architecture comes at the cost of additional analog overhead, increased parasitics, and frontend-sampler matching issues.

B. Proposed Narrowband-Dither-Based Calibration

To overcome the aforementioned issues, we propose an alternative method based on narrowband dither injection. This is depicted by the spectrum in Fig. 6(c) [and flag use narrowband dither = "1" in Fig. 6(a)]. As shown in this figure, the dither is injected in a narrow band that does not overlap with the input signal band, and is isolated at the ADC output using a digital bandpass filter (BPF) centered at the injection band. This allows for reliable tracking of dither-correlated energy and permits the use of an integration constant μ that provides fast estimation, while avoiding the complications of the auxiliary-ADC and split-ADC implementations.

The convergence speed of the proposed algorithm depends on the ratio of the dither-correlated power to other uncorrelated power (including the signal power) at the integrator input. This has to be taken into account when considering the location
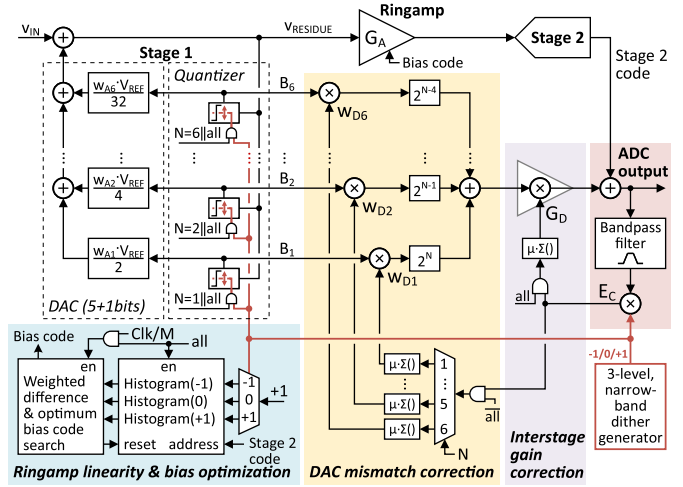

Fig. 7.   Implemented calibration engines (color-shaded blocks implemented off-chip; power-detector-based control of Fig. 6(a) omitted for simplicity).

of the dither band and its bandwidth. Under the assumptions of ideal bandpass filtering, uniformly-distributed dither power (non-overlapping with the signal) and white noise, this "dither-correlated-power-to-other-power" ratio is independent of the dither bandwidth size. In practice, however, the largest contributor to the estimation noise is the input signal itself through its leakage to the integrator input due to non-ideal filtering. Hence, a sharp and narrow BPF which cancels as much signal leakage as possible is preferred. From another perspective, a narrow dither bandwidth is also preferred so that most the spectrum can be used for the input signal. This naturally comes at the cost of digital power and area (i.e., more taps are necessary to realize a sharper filter profile).

An important consideration for the practical implementation of the proposed algorithm is the potential overlap between the input signal and the dither band due to variation of the signal spectrum across time. As shown in Fig. 6(a), this can be addressed by means of a digital power detector at the BPF output, which measures the power in the dither band (based on an estimation of the RMS value of the digital BPF output). This power is ideally composed exclusively of dither, and its approximate expected level is known (and can be simulated). Any excess power must come from the input signal, and achieves a maximum when the signal and dither bands fully overlap. Based on the information provided by the power detector, the estimation error (i.e., μ) can be adjusted automatically. Alternatively, the dither band can be moved to a different location (after a programmable time-out), effectively implementing a search for a band without signal power that can be used for dither injection. Critically, any non-ideal overlap of signal and dither bands will affect the convergence speed of the estimator, but convergence is ultimately always guaranteed independent of signal characteristics and/or filter configuration. Likewise, any mismatch between the dither injection and extraction filters affects only convergence speed due to lost dither power, but not convergence itself.

The proposed approach is used in this work to implement the interstage-gain and DAC-mismatch calibration engines shown in Fig. 7, as described in Sections III-C–III-E.

C. Interstage-Gain Calibration

As described in Section II, this work exploits a quantizer capable of per-bit dither injection. Based on a three-level PN dither sequence, the Stage-1 quantization thresholds can be either fixed to a nominal position (dither code 0) or offset to some positive or negative value (dither codes $+1$ and -1, respectively), as shown in Fig. 7. For interstage-gain calibration, a common dither value must be used in all thresholds within a single conversion cycle (control signal all = "1"). For DAC mismatch calibration only one of the thresholds within a conversion cycle is dithered (signaled by the control signal N), while all the other remain in their nominal position (all = "0").

In the presence of a gain error, i.e., when $G_A \neq G_D$ (we initially assume no DAC mismatch: $w_{A,i} = w_{D,i} = 1$), the injected quantizer-threshold dithering signal induces an error during the Stage-1 SAR conversion. This error is tracked in the narrow band of interest, which is isolated at the ADC output by a digital bandpass FIR filter, and used in an LMS-based correction loop (implemented off-chip in MATLAB). Power-detector-based adjustment of the convergence rate (scaling factor μ) is continuously active in the background, to ensure reliable estimation independently of the relationship between the signal and the dither bandpass positions (the power detector is omitted in Fig. 7 for simplicity).

In this design, the BPF passband is set to roughly 5% of the available Nyquist band. A 32-tap FIR filter is used both in the dither injection (implemented on-chip) and in the dither extraction at the ADC output (implemented off-chip). With a value for μ chosen such that estimation noise has no significant impact on the results, an initial uncorrected 5% interstage-gain error can be calibrated within $\sim$350 kcycle, as shown in Fig. 8(a). A convergence-speed comparison with the prior-art wideband dither technique is also shown in Fig. 8(b). More than two orders of magnitude in speed enhancement are achieved with the proposed narrowband technique, when the signal is well isolated from the dither band. Finally, Fig. 8(c) shows a sweep of the BPF center frequency for a fixed input signal (for multiple ADC output-data captures). The algorithm reliably estimates the interstage gain thanks to the power-detector-based scaling of μ, which is adaptively adjusted to provide sufficient attenuation of the signal-induced error in the gain estimation when the signal and dither bands overlap.

D. DAC Mismatch Calibration

When random capacitor mismatch is present in the Stage-1 DAC, the corresponding bit weights do not follow binary scaling anymore (i.e., $w_{A,i} \neq 1$ in Fig. 7). Just as with the interstage-gain error, DAC mismatch effects are nulled during digital reconstruction when the reconstruction coefficients accurately match their analog counterparts, $w_{A,i} = w_{D,i}$ (assuming $G_D = G_A$). As shown in Fig. 7, this design also uses narrowband-dither-based calibration to estimate the optimal reconstruction coefficients $w_{D,i}$. The DAC bit weights are calibrated sequentially, starting from the MSB. Only one of the comparisons within a quantization cycle is dithered at a time (e.g., $N = 1$ for calibration of the MSB), while all others remain in their nominal position (all = "0"). In this
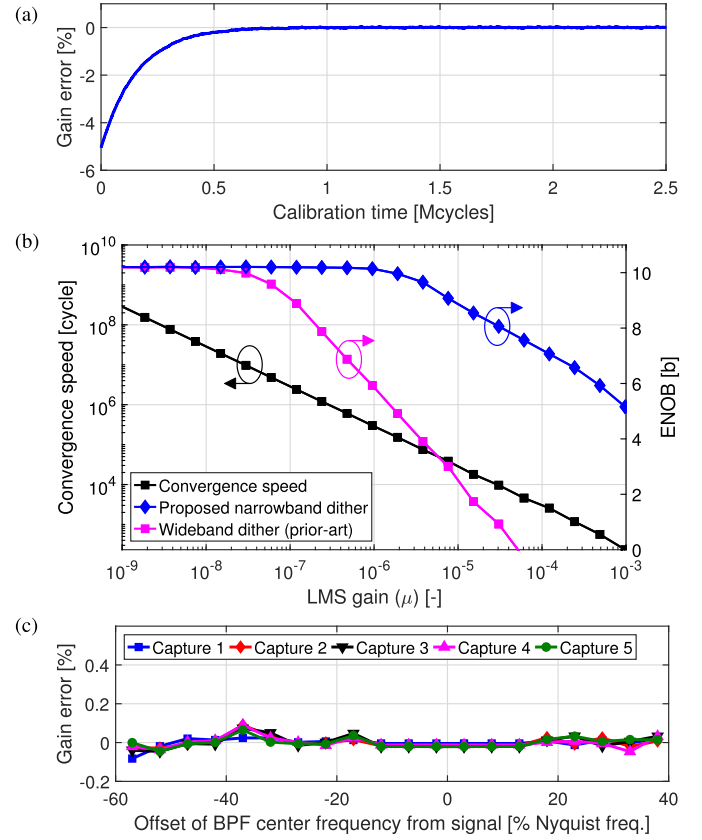

Fig. 8. Measured interstage-gain estimation. (a) Convergence speed. (b) Convergence speed comparison with wideband dither injection. (c) Gain estimation error for variable BPF center frequency (and fixed v_{IN} location).
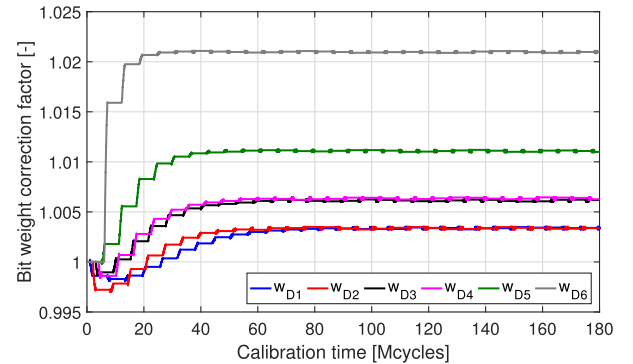

Fig. 9. Measured estimation of the optimal reconstruction coefficients $w_{D,i}$.

way, it is possible to independently track the dither-correlated energy present at the ADC output for each DAC capacitor. The correction mechanism and its convergence speed are similar to that of the interstage-gain calibration, as shown[1] in Fig. 9.

Note that the DAC mismatch relates to MOM capacitor mismatch, which is insensitive to environmental variations (e.g., changes in temperature and supply voltage). Therefore,

---

[1] The "staircase" shape of the convergence curves in Fig. 9 results from the particular implementation of the calibration algorithm, in which the bit weights are not estimated using single attempts but following an iterative procedure: each weight is estimated during a fixed number of cycles and then held, and after all the weights have been estimated, the process is repeated.
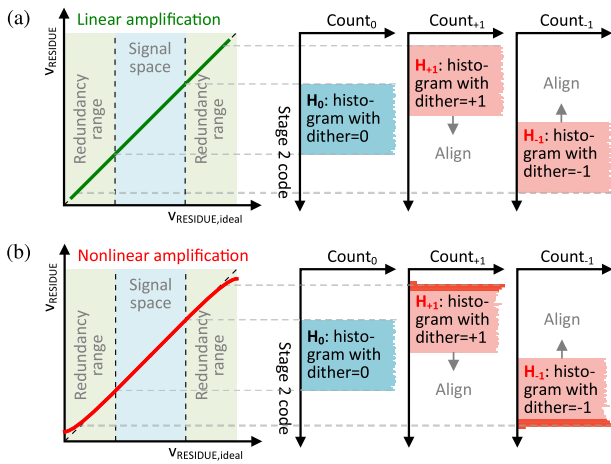
Fig. 10. Nonlinearity estimation based on backend-code histogram analysis. (a) Linear and (b) nonlinear amplification of a uniformly-distributed input.
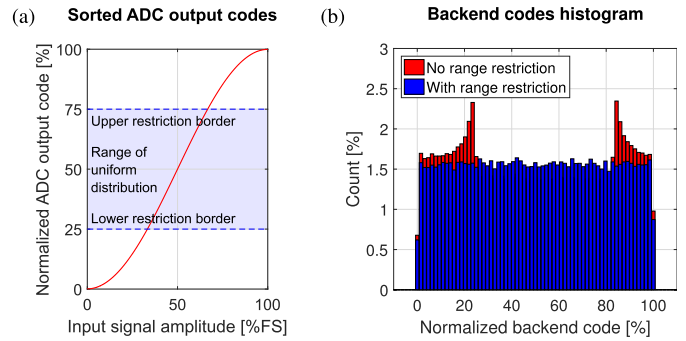

Fig. 11. (a) Range restriction concept for uniformization of the backend histograms under sinusoidal-input excitation and (b) backend code histograms.

the mismatch calibration engine estimating $w_{D,i}$ needs to operate only at chip startup (with interstage-gain calibration initially disabled). After all the $w_{D,i}$ are estimated, they remain fixed and the interstage-gain calibration takes over.

As discussed in Section II-B, the proposed dither injection method requires negligible analog overhead. Varying the quantizer thresholds is simple, and there is no direct critical-timing limitation (quantizer offsets can be programmed while the stage is tracking its input). Another important advantage is robustness to analog inaccuracies. This stems from the fact that the dither is injected into the analog signal path in the form of quantization error [24]. When the optimal digital reconstruction coefficients are known, the digital redundancy of the system cancels this quantization error. Thus, the absolute accuracy of the injected dither is irrelevant for the convergence or accuracy of the proposed calibration algorithms, and as long as redundancy bounds are not exceeded and as long as the offsets introduced in the quantization thresholds vary monotonically with the logic dither values (-1, 0, $+1$), there are no matching or analog precision requirements for the calibration hardware to operate robustly across PVT variations.

E. Residue-Amplifier Linearity and Bias Optimization

By exploiting the proposed quantizer and the injected three-level dither, linearity and bias optimization of the residue amplifier can also be performed in the background at no extra analog hardware cost. The method, illustrated in Fig. 10, is based on the analysis of the backend code histograms that result for each applied dither value. For now, let us assume that the statistical distribution of the analog residue generated by Stage 1 is uniform and bounded to 1 LSB. In the case of perfectly-linear amplification, the amplified residue and the Stage-2 code histogram will also be uniformly distributed. Injecting dither through the Stage-1 quantizer will shift the Stage-2 histogram by a fixed value, using some of the interstage redundancy range. Critically, this does not change the uniform shape of the Stage-2 histogram, only its offset [see Fig. 10(a)]. Now, let us consider the practical case of nonlinear amplification. Since each dither code induces a different

offset in the amplified residue, the latter experiences different nonlinear transformations, and this distortion is captured in the Stage-2 histogram. For example, in the case of compressive nonlinearity [see Fig. 10(b)], the compression at the edges of the amplifier output range will cause the histograms for the $+1$ and -1 dither cases to be more nonuniform than the zero-dither case that lies in the central, less-compressed region. From these thought experiments, the main principle of the proposed technique emerges: the more linear the amplifier, the more invariant the Stage-2 histogram shape will be to dither.
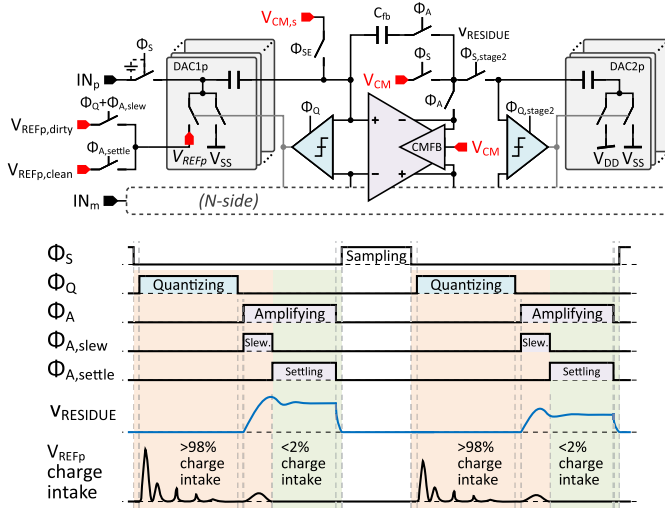
Practical implementation involves injecting a three-level PN dither sequence into the Stage-1 quantizer and then sorting the Stage-2 output codes into three histograms according to the injected dither values. To calculate an estimate of the amplifier nonlinearity, the histograms are first aligned for maximum correlation. Then we compute the metric

$$\text{NL} = \sum (H_0 \times |H_{+1} - H_0| + H_0 \times |H_{-1} - H_0|) \quad (1)$$

which involves: 1) calculating the absolute differences between histograms, bin-by-bin (these differences are smaller with linear amplification); 2) scaling the differences by the non-dithered-histogram bin values; and 3) summing all the products to create a single nonlinearity metric: NL. This value serves as an indicator of the degree of amplification nonlinearity present and can be used as an objective function to optimize the residue amplifier biasing so that NL → 0.

For reliable NL estimation, the input signal must preferably be uniformly distributed, which is typically true for realistic communication channels. In the presence of a deterministic sinusoidal excitation (typically used for testing purposes in the laboratory), this is no longer the case. An example of a backend histogram for such a case is depicted on Fig. 11(b) (red histogram). Codes corresponding to the peaks of the sine wave are excited more frequently, resulting in a characteristic spiking in the histogram.[2] This nonuniform histogram profile can degrade the accuracy of the NL estimate. To overcome this issue, we restrict the range of ADC output codes for which backend histogram information is collected. As shown in Fig. 11(a), the histogram is updated only for the center half of the ADC output range, where the codes distribute

---

[2]Note that since Stage 1 operates with a redundant LSB decision [34], the spiking "folds" within the histogram itself and it does not appear at its edges.

Fig. 12. Regulated reference voltages and V_{REFp} charge intake details.

Fig. 13. Detailed implementation of the proposed on-chip reference regulator.

uniformly. This effectively achieves uniformization of the backend histogram, as shown in Fig. 11(b) (blue histogram), and ensures accurate NL estimation. To support any ADC input signal amplitude, the restriction range is scaled to the power of the measured signal, and is set empirically. Choosing a 20% larger/smaller range does not have a significant impact on the measured results. Although the proposed calculation method is not 100% "foolproof" for any possible input signal, it is largely adequate to show the capability of the dither-based nonlinearity estimation. Further developments to ensure robustness for all input signals are left for future work.

The presented technique is agnostic to the particular method of residue amplification, and can be used for background-optimization of any programmable amplifier. In this work, it is used to set the bias voltages ($V_{BIAS,H}$ and $V_{BIAS,L}$ in Fig. 1) that define the ringamp settling behavior [22]. The technique relies purely on signal statistics (which are preferably constant in the time span of histogram collection), and is independent of clock and input signal frequencies. It also averages random noise, and as such, NL is representative of the SDR in the system, which might not be directly proportional to the SNDR.

The practical realization of the proposed mechanism requires a digital engine capable of calculating backend-code histograms for each dither level and per-bin arithmetic operations (such as subtraction and multiplication), whose implementation is out of the scope of this work. As noted in Fig. 7, in our implementation this processing is executed off-chip.

IV. ON-CHIP REFERENCE REGULATION

As shown in Fig. 12, the proposed ADC operates using analog references V_{REFp}, V_{CM}, and V_{CMs}. These references are regulated exploiting an on-chip, fully-dynamic reference regulator based on [15], improved for the pipelined-SAR architecture. Core implementation differences to prior art include: 1) hybrid (pumping + sharing) charge-return control to support arbitrary reference-voltage values; 2) exclusion of a V_{REFm} reference for power/area savings, along with the
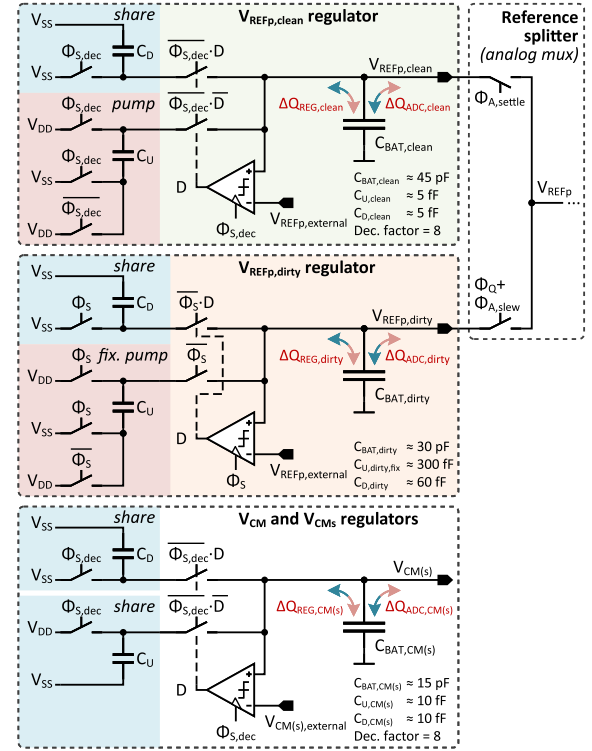
necessary adjustments to accommodate for its omission; and 3) implementation details for improved regulation efficiency.

As illustrated in Fig. 12, the basic principle of Split-Reference Regulation is to exploit the usual inverse relationship between the amount of instantaneous reference charge delivered to a circuit and the required reference accuracy at that same point in time [15]. The main reference of the ADC, V_{REFp}, is for that purpose split in two replicas, $V_{REFp,dirty}$ and $V_{REFp,clean}$. A substantial amount of (code dependent) charge is sourced from V_{REFp} during the quantization phase ϕ_Q (when the Stage-1 SAR quantizes) and during the initial phase of residue amplification $\phi_{A,slew}$ (when charge is pulled from the reference by the capacitive feedback circuit). Notably, any error due to inaccuracy in the reference during these two phases ($\phi_Q + \phi_{A,slew}$) is absorbed by redundancy in the system architecture. Thus, an analog mux connects $V_{REFp,dirty}$ to the frontend DAC during $\phi_Q + \phi_{A,slew}$. Regulation of this replica must accommodate large charge intake, but it requires only low precision.

By contrast, throughout the second phase of amplification, $\phi_{A,settle}$, the ringamp output voltage is only changing very slightly, and charge intake from the connected reference is minor. The reference accuracy, however, is at this point most critical. Like the accuracy of the feedback settling itself, any error in the applied reference will translate into an error in the amplified residue passed onto Stage 2 for further quantization. Thus, the analog mux connects $V_{REFp,clean}$ to the DAC during $\phi_{A,settle}$. Regulation of this replica must accommodate only a small charge intake, but it requires high precision.

Fig. 13 details the actual implementation of the proposed regulator. A single analog mux with non-overlapping control,

outside of the ADC core, connects the Stage-1 DAC to either of the V_{REFp} replicas. The layout is optimized to avoid excessive parasitic capacitance on the V_{REFp} node because charge left here after $V_{\text{REFp,dirty}}$ is disconnected creates an error-transfer path from the dirty to the clean replica. Separate C_{BAT} capacitors act as batteries, limiting the maximum voltage ripple that can occur on the V_{REFp} replicas and the common-mode references V_{CM} and V_{CMs}. The charge sourced/sunk from/to each C_{BAT} is dynamically replenished by simple digital control loops[3] that are optimized for the opposing charge delivery and precision requirements of each replica. The "dirty" regulator has a big charge pump that can deliver the required charge, whereas the "clean" regulator has a small pump for fine and accurate control. A similar regulator is implemented for the references V_{CM} and V_{CMs}, but because of their relaxed accuracy requirements, no dirty/clean split is necessary. As in [15], the option to skip clock cycles and "decimate" the digital regulation loop for additional power savings is included in the $V_{\text{REFp,clean}}$ and $V_{\text{CM}(s)}$ replicas, due to their very low charge-delivery requirements.

To pull the regulated voltages up/down, charge from the C_{BAT} reservoirs is shared with the C_U/C_D capacitors, respectively, with an exception in the regulation of the V_{REFp} replicas. To pull the V_{REFp} replicas up, charge pumping (instead of charge sharing as in [15]) is used. To this purpose, the capacitor C_U is initially precharged to V_{DD}, and in the charge return phase, when its top plate connects to C_{BAT}, its bottom plate is connected to V_{DD}. This charge pumping method enables the V_{REFp} regulator to synthesize any voltage within the supply limits (and even beyond), unlike charge sharing, which is confined to a narrower range of voltages that notably does not include levels at and around V_{DD}.

Due to the specific implementation of the Stage-1 SAR in this design, not only is the charge intake from $V_{\text{REFp,dirty}}$ always unidirectional, but also a large portion of it is signal-independent. This presents an opportunity to relax the ripple-versus-charging-capacity tradeoff [15] for the $V_{\text{REFp,dirty}}$ regulator. Specifically, C_U in this regulator is sized to pump charge into $C_{\text{BAT,dirty}}$ at every cycle regardless of the comparator decision, providing slightly more charge than what is taken on average by the ADC. When $V_{\text{REFp,dirty}}$ drifts above its target level, due to signal-dependent effects or otherwise, the comparator uses C_D to pull some corrective charge out of $C_{\text{BAT,dirty}}$ (note that $C_U \approx 5C_D$). Thus, the $V_{\text{REFp,dirty}}$ regulator must only compensate the fluctuations in charge pull, and not for the much larger absolute charge pull.

As shown in Fig. 12, this design uses V_{SS} as the negative reference. This reduces the required battery size (by $3.5\times$ compared to [15]) and the regulation power. However, to avoid potential common-mode imbalance issues during residue amplification when the required V_{REFp} is lower than V_{DD}, the sampling common-mode reference V_{CMs} is regulated separately (see Fig. 12). Thus, setting $V_{\text{CMs}} = V_{\text{DD}} - V_{\text{REFp}}/2$ (assuming that the input signal common-mode is set mid-rail:

Fig. 14. Chip microphotograph.

Fig. 15. Interstage-gain calibration: measured ENOB versus supply voltage.

$V_{\text{CMi}} = V_{\text{DD}}/2$) ensures that the input common-mode of the residue amplifier remains at mid-rail during amplification, as required for optimal operation. Finally, since a well-balanced differential structure is resilient to common-mode noise, the V_{CM} and V_{CMs} regulators can operate with very relaxed requirements, without dirty/clean splitting and comparably smaller C_{BAT} sizes, and at a decimated clock rate. Also, there is no need for charge pumping in the regulation of these references, as they typically require voltages close to mid-rail.

V. MEASUREMENT RESULTS

The ADC is implemented in a 1P11M 16-nm FinFET CMOS process. The ADC core occupies an active area of 0.0084 mm^2 (75 μm $\times$ 112 μm) and the reference regulator 0.032 mm^2 (200 μm $\times$ 160 μm). Only SVT/ULVT core devices are employed in the implementation of these blocks. A die photograph is shown in Fig. 14.

All the results herein reported are obtained from a single die sample and using reconstruction coefficients estimated by the calibration engines described in Sections III-C and III-D. Fig. 15 illustrates the ability of the proposed interstage-gain calibration to successfully track supply-induced gain variations. All the chip settings remain constant throughout this experiment, nominally set for optimal performance at $V_{\text{DD}} = 0.9$ V. The ADC is in this experiment runs at a lower clock rate (200 MS/s) to ensure functionality down to $V_{\text{DD}} = 0.8$ V. Without background estimation of the interstage gain, which is sensitive to the supply dc level, and due to the particular ringamp dead-zone biasing method employed [22], varying V_{DD} without adjusting G_D results in substantial performance degradation. With background calibration enabled, however, this issue is fully resolved and the ADC operates at its nominal performance.

---

[3]In the implemented prototype the offsets of the comparators used in these control loops are compensated in a foreground calibration step to minimize any static offset between the clean and dirty replicas, which could otherwise increase both the regulation error and the charge intake of the clean replica.
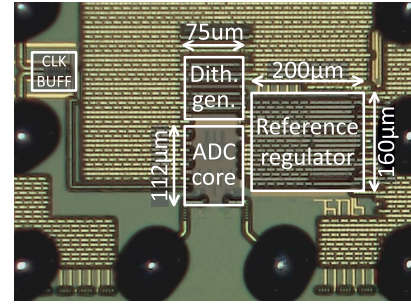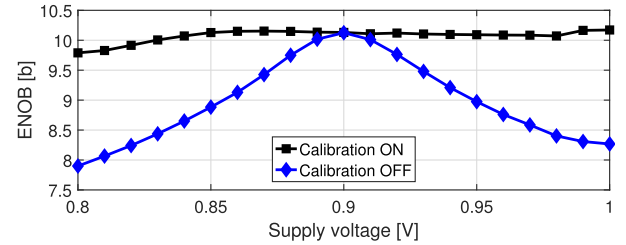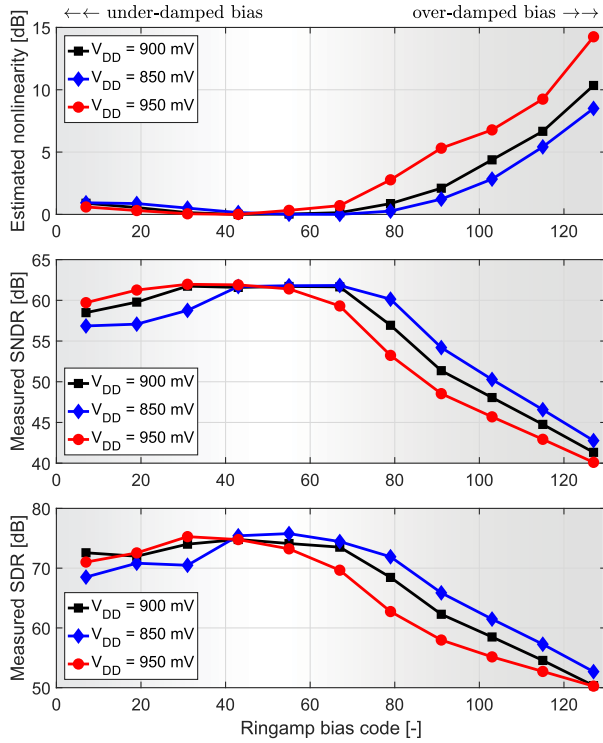
Fig. 16. Residue amplifier linearity and bias optimization: estimated nonlinearity (NL), measured SNDR and measured SDR versus ringamp bias code.
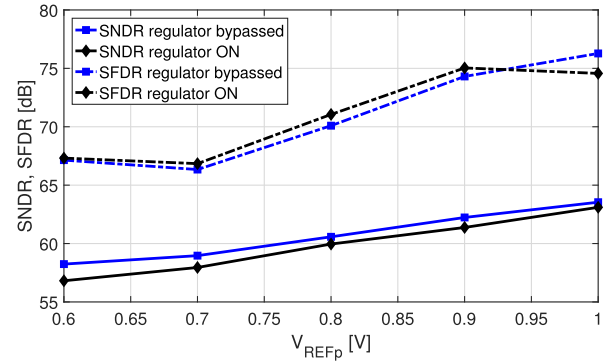

Fig. 17. Measured performance versus V_{REFp} with and without regulation.
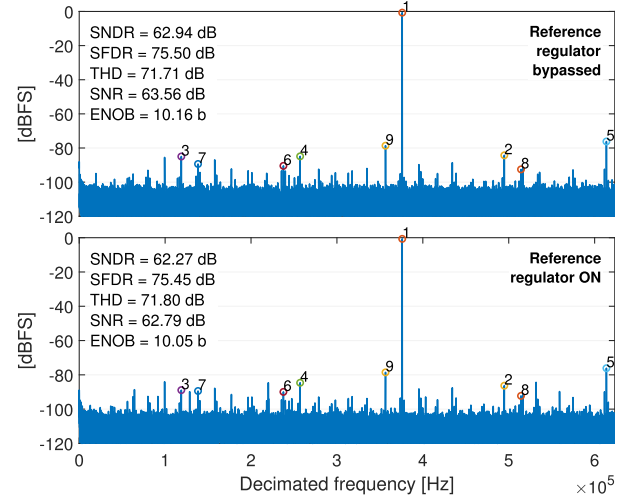

Fig. 18. Measured output spectra with and without reference regulation (500 MS/s; -0.5 dB$_{FS}$ near-Nyquist input; $N_{dec} = 401$).

Fig. 16 shows the measurement results of the background ringamp linearity and bias optimization using the approach described in Section III-E. It presents a sweep of ringamp bias-DAC codes versus the computed NL estimate, along with the measured S(N)DR. The experiment is repeated at different V_{DD} levels (0.85, 0.90, and 0.95 V) to verify the ability of the algorithm to find optimal biasing in the presence of supply variations that alter the ringamp settling by changing the internal dead-zone that defines its transient response. An over-damped biasing of the amplifier results in excess settling error in the available amplification time, as visible toward the right-hand side of Fig. 16 (codes above the optimum bias values). Likewise, an under-damped biasing of the ringamp also results in excess settling error, as visible on the left-hand side of Fig. 16 (codes below the optimum bias values). Both of these biasing extremes degrade the amplification linearity and consequentially the measured S(N)DR. By leveraging the proposed nonlinearity-estimation algorithm, the ringamp can always be re-biased in the optimal plateau of codes that provide minimal distortion and maximal SNDR.

Fig. 17 illustrates the ability of the on-chip reference regulator to synthesize a wide range of V_{REFp} values. In these measurements V_{DD} is kept constant and the input signal power is scaled to maintain -1 dB$_{FS}$ at every point to avoid saturation. Also, the internally-regulated V_{CMs} is adjusted to accommodate for the varying V_{REFp}, as discussed in Section IV. The ADC operates reliably and with minimal impact on performance irrespective of whether regulation is enabled or bypassed (the performance loss observed as the value of V_{REFp} is reduced is

simply a consequence of the smaller full-scale signal swing and SNR).

Fig. 18 shows the measured output spectra both with and without (i.e., bypassed) reference regulation for the ADC running at 500 MS/s with a -0.5 dB$_{FS}$, near-Nyquist input. It can be seen that the reference regulation has very small impact on performance, yielding 10.1 ENOB and 75.5 dB SFDR under these conditions. The measured performance versus clock and input frequency is further illustrated in Fig. 19. These results confirm that the reference regulation is robust against signal-dependent effects such as clock/input beat-frequencies, and that the background calibration is able to operate independently of clock and signal frequencies as well. The maximum sampling rate is 500 MS/s and the ERBW is about 900 MHz.

The ADC performance is summarized in Fig. 20. Operating entirely from a 0.9-V supply, the ADC consumes 3.3 mW at 500 MS/s, of which 2.8 mW are consumed by the core and 0.5 mW by the reference regulator, yielding Walden and Schreier FoM values of 6.2 fJ/conv.-step and 171.1 dB, respectively. Thanks to its fully-dynamic operation, the ADC power consumption scales linearly with clock frequency.
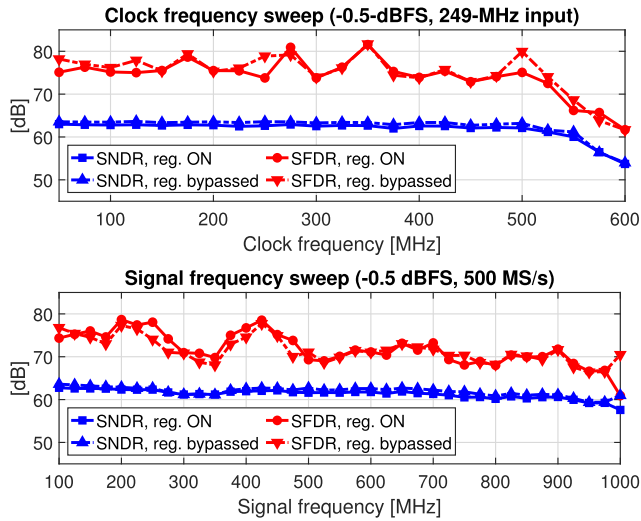
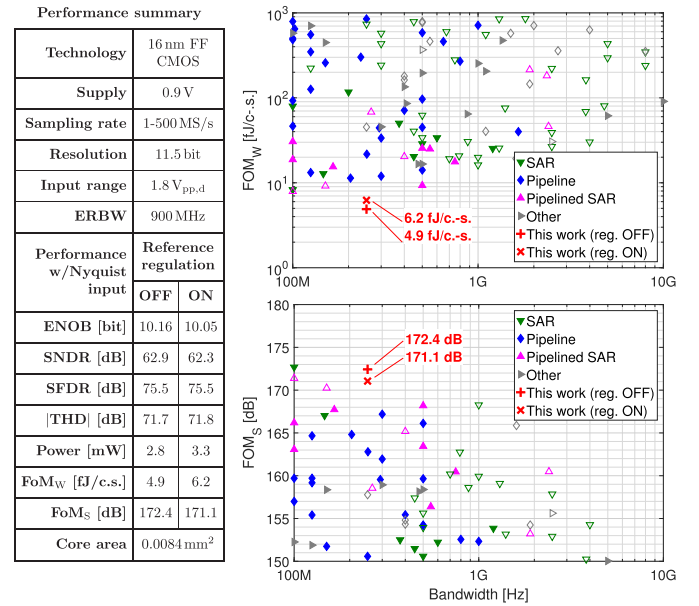Fig. 19. Frequency sweeps with and without reference regulation.

Fig. 20. Performance summary (left) and Walden and Schreier FoM comparison (right) with the ADCs published at ISSCC & VLSI conferences from 1997 to 2021 [1] (unfilled symbols denote implementations using time-interleaving).

VI. Conclusion

This work achieves the highest power efficiency reported to-date among all single-channel ADCs of any architecture operating above 200 MS/s, as shown in Fig. 20 [1]. This achievement is largely made possible by the availability of a high-efficiency ringamp residue amplifier that can support any input amplitude, produce a large and programmable interstage gain, and generate a large-amplitude, linear output residue. This, in turn, decouples and relaxes the design tradeoffs of the Stage-1 and Stage-2 SAR sub-ADCs significantly.

Many of the key contributions in this work can be generalized. Narrowband dither injection offers a means of increasing convergence speed and/or estimation accuracy in many types of dither-based calibration systems. Likewise, the multi-latch SAR quantizer provides a dither-compatible solution that can be used in many SAR topologies, without sacrificing performance. Although the ringamp in this design received little direct attention, it is a key motivation behind the exclusively-dither-based approach to calibration in this system. Unlike other ringamp-bias optimization solutions requiring extra analog hardware [15], [16], this work reuses the dithering capabilities that would anyway be included in the system to calibrate other errors. Moreover, the same approach could also be applied to linearity enhancement in other residue amplifiers (e.g., G_m-C and G_m-R). Future-work possibilities include alternative approaches and algorithms for dither-based amplifier linearity estimation, both histogram-based and otherwise.

The reference regulation system presented here provides a more versatile implementation of the Split-Reference Regulation concept than the original in [15], free from constraints on reference voltage value. Noting that the same principles are applicable to stand-alone SARs by connecting different replicas during MSB and LSB conversions, it can be seen that the concept works in switched (e.g., SAR), residue-amplification (e.g., pipeline and delta sigma), and mixed (e.g., pipelined SAR) contexts. Future-work opportunities include exploring techniques to reduce the reservoir capacitor size/area.

This design adds to a growing list of ringamp-based ADCs reported in recent years that advance the state-of-the-art in power efficiency across a broad range of target accuracies and speeds. With regard to other previously-reported ringamp-based pipelined SARs, it significantly improves upon the maximum per-channel sampling speed achieved.

References

[1] B. Murmann. (2021). *ADC Performance Survey 1997–2021*. [Online]. Available: http://web.stanford.edu/~murmann/adcsurvey.html

[2] G. V. D. Plas and B. Verbruggen, "A 150 MS/s 133 μW 7 bit ADC in 90 nm digital CMOS," *IEEE J. Solid-State Circuits*, vol. 43, no. 12, pp. 2631–2640, Dec. 2008.

[3] B. Verbruggen, M. Iriguchi, and J. Craninckx, "A 1.7 mW 11 b 250 MS/s 2-times interleaved fully dynamic pipelined SAR ADC in 40 nm digital CMOS," *IEEE J. Solid-State Circuits*, vol. 47, no. 12, pp. 2880–2887, Dec. 2012.

[4] T. Jiang, W. Liu, F. Y. Zhong, C. Zhong, K. Hu, and P. Y. Chiang, "A single-channel, 1.25-GS/s, 6-bit, 6.08-mW asynchronous successive-approximation ADC with improved feedback delay in 40-nm CMOS," *IEEE J. Solid-State Circuits*, vol. 47, no. 10, pp. 2444–2453, Oct. 2012.

[5] Z. Cao, S. Yan, and Y. Li, "A 32 mW 1.25 GS/s 6b 2b/step SAR ADC in 0.13 μm CMOS," *IEEE J. Solid-State Circuits*, vol. 44, no. 3, pp. 862–873, Feb. 2009.

[6] H. Wei *et al.*, "An 8-b 400-MS/s 2-b-per-cycle SAR ADC with resistive DAC," *IEEE J. Solid-State Circuits*, vol. 47, no. 11, pp. 2763–2772, Nov. 2012.

[7] C.-H. Chan, Y. Zhu, W.-H. Zhang, U. Seng-Pan, and R. P. Martins, "A two-way interleaved 7-b 2.4-GS/s 1-then-2 b/cycle SAR ADC with background offset calibration," *IEEE J. Solid-State Circuits*, vol. 53, no. 3, pp. 850–860, Mar. 2018.

[8] E. Martens, B. Hershberg, and J. Craninckx, "A 69-dB SNDR 300-MS/s two-time interleaved pipelined SAR ADC in 16-nm CMOS FinFET with capacitive reference stabilization," *IEEE J. Solid-State Circuits*, vol. 53, no. 4, pp. 1161–1171, Apr. 2018.

[9] B. Vaz *et al.*, "A 13 b 4 GS/s digitally assisted dynamic 3-stage asynchronous pipelined-SAR ADC," in *IEEE Int. Solid-State Circuits Conf. (ISSCC) Dig. Tech. Papers*, Feb. 2017, pp. 276–277.

[10] W. Jiang, Y. Zhu, M. Zhang, C.-H. Chan, and R. P. Martins, "A temperature-stabilized single-channel 1-GS/s 60-dB SNDR SAR-assisted pipelined ADC with dynamic Gm-R-based amplifier," *IEEE J. Solid-State Circuits*, vol. 55, no. 2, pp. 322–332, Feb. 2020.

The performance summary table (center):

Performance summary	
Technology	16 nm FF CMOS
Supply	0.9 V
Sampling rate	1-500 MS/s
Resolution	11.5 bit
Input range	1.8 $V_{pp,d}$
ERBW	900 MHz

Performance w/Nyquist input	Reference regulation	
	OFF	ON
ENOB [bit]	10.16	10.05
SNDR [dB]	62.9	62.3
SFDR [dB]	75.5	75.5
|THD| [dB]	71.7	71.8
Power [mW]	2.8	3.3
FoM$_W$ [fJ/c.s.]	4.9	6.2
FoM$_S$ [dB]	172.4	171.1
Core area	0.0084 mm^2	

[11] B. Verbruggen *et al.*, "A 2.1 mW 11b 410 MS/s dynamic pipelined SAR ADC with background calibration in 28 nm digital CMOS," in *Proc. Symp. VLSI Circuits*, Jun. 2013, pp. C268–C269.

[12] S. Liu, H. Han, Y. Shen, and Z. Zhu, "A 12-bit 100-MS/s pipelined-SAR ADC with PVT-insensitive and gain-folding dynamic amplifier," *IEEE Trans. Circuits Syst. I, Reg. Papers*, vol. 67, no. 8, pp. 2602–2611, Aug. 2020.

[13] B. Hershberg, S. Weaver, K. Sobue, S. Takeuchi, K. Hamashita, and U.-K. Moon, "Ring amplifiers for switched capacitor circuits," *IEEE J. Solid-State Circuits*, vol. 47, no. 12, pp. 2928–2942, Dec. 2012.

[14] J. Lagos, B. P. Hershberg, E. Martens, P. Wambacq, and J. Craninckx, "A 1-GS/s, 12-b, single-channel pipelined ADC with dead-zone-degenerated ring amplifiers," *IEEE J. Solid-State Circuits*, vol. 54, no. 3, pp. 646–658, Mar. 2019.

[15] B. Hershberg, N. Markulic, J. Lagos, E. Martens, D. Dermit, and J. Craninckx, "A 1-MS/s to 1-GS/s ringamp-based pipelined ADC with fully dynamic reference regulation and stochastic scope-on-chip background monitoring in 16 nm," *IEEE J. Solid-State Circuits*, vol. 56, no. 4, pp. 1227–1240, Apr. 2021.

[16] B. Hershberg *et al.*, "A 4-GS/s 10-ENOB 75-mW ringamp ADC in 16-nm CMOS with background monitoring of distortion," *IEEE J. Solid-State Circuits*, vol. 56, no. 8, pp. 2360–2374, Aug. 2021.

[17] Y. Lim and M. P. Flynn, "A 1 mW 71.5 dB SNDR 50 MS/s 13 bit fully differential ring amplifier based SAR-assisted pipeline ADC," *IEEE J. Solid-State Circuits*, vol. 50, no. 12, pp. 2901–2911, Dec. 2015.

[18] Y. Lim and M. P. Flynn, "A calibration-free 2.3 mW 73.2 dB SNDR 15 b 100 MS/s four-stage fully differential ring amplifier based SAR-assisted pipeline ADC," in *Proc. Symp. VLSI Circuits*, Jun. 2017, pp. C98–C99.

[19] A. ElShater *et al.*, "A 10-mW 16-b 15-MS/s two-step SAR ADC with 95-dB DR using dual-deadzone ring amplifier," *IEEE J. Solid-State Circuits*, vol. 54, no. 12, pp. 3410–3420, Oct. 2019.

[20] J.-C. Wang, T.-C. Hung, and T.-H. Kuo, "A calibration-free 14-b 0.7-mW 100-MS/s pipelined-SAR ADC using a weighted-averaging correlated level shifting technique," *IEEE J. Solid-State Circuits*, vol. 55, no. 12, pp. 3271–3280, Dec. 2020.

[21] J. Lagos *et al.*, "A 10.0 ENOB, 6.2 fJ/conv.-step, 500 MS/s ringamp-based pipelined-SAR ADC with background calibration and dynamic reference regulation in 16 nm CMOS," in *Proc. Symp. VLSI Circuits*, Jun. 2021, pp. 1–2.

[22] J. Lagos, B. Hershberg, E. Martens, P. Wambacq, and J. Craninckx, "A single-channel, 600-MS/s, 12-b, ringamp-based pipelined ADC in 28-nm CMOS," *IEEE J. Solid-State Circuits*, vol. 54, no. 2, pp. 403–416, Feb. 2019.

[23] B. Hershberg *et al.*, "Asynchronous event-driven clocking and control in pipelined ADCs," *IEEE Trans. Circuits Syst. I, Reg. Papers*, vol. 68, no. 7, pp. 2813–2826, Jul. 2021.

[24] J. Li and U.-K. Moon, "Background calibration techniques for multi-stage pipelined ADCs with digital redundancy," *IEEE Trans. Circuits Syst. II, Analog Digit. Signal Process.*, vol. 50, no. 9, pp. 531–538, Sep. 2003.

[25] H. Pan and A. A. Abidi, "Spectral spurs due to quantization in Nyquist ADCs," *IEEE Trans. Circuits Syst. I, Reg. Papers*, vol. 51, no. 8, pp. 1422–1439, Aug. 2004.

[26] C. Zhu, R. Liang, J. Lin, Z. Wang, and L. Li, "Analysis and design of a large dither injection circuit for improving linearity in pipelined ADCs," *IEEE Trans. Very Large Scale Integr. (VLSI) Syst.*, vol. 27, no. 9, pp. 2008–2020, Sep. 2019.

[27] C.-C. Liu, S.-J. Chang, G.-Y. Huang, and Y.-Z. Lin, "A 10-bit 50-MS/s SAR ADC with a monotonic capacitor switching procedure," *IEEE J. Solid-State Circuits*, vol. 45, no. 4, pp. 731–740, Apr. 2010.

[28] P. Harpe, C. Zhou, X. Wang, G. Dolmans, and H. de Groot, "A 30 fJ/conversion-step 8 b 0-to-1 0MS/s asynchronous SAR ADC in 90 nm CMOS," in *IEEE Int. Solid-State Circuits Conf. (ISSCC) Dig. Tech. Papers*, Feb. 2010, pp. 388–389.

[29] Y.-Z. Lin, C.-H. Tsai, S.-C. Tsou, and C.-H. Lu, "A 8.2-mW 10-b 1.6-GS/s 4×TI SAR ADC with fast reference charge neutralization and background timing-skew calibration in 16-nm CMOS," in *Proc. IEEE Symp. VLSI Circuits (VLSI-Circuits)*, Jun. 2016, pp. 1–2.

[30] H. Xu and A. A. Abidi, "Analysis and design of regenerative comparators for low offset and noise," *IEEE Trans. Circuits Syst. I, Reg. Papers*, vol. 66, no. 8, pp. 2817–2830, Aug. 2019.

[31] P. Nuzzo, C. Nani, C. Armiento, A. Sangiovanni-Vincentelli, J. Craninckx, and G. Van der Plas, "A 6-bit 50-MS/s threshold configuring SAR ADC in 90-nm digital CMOS," *IEEE Trans. Circuits Syst. I, Reg. Papers*, vol. 59, no. 1, pp. 80–92, Jan. 2012.

[32] P. Nuzzo, F. De Bernardinis, P. Terreni, and G. Van der Plas, "Noise analysis of regenerative comparators for reconfigurable ADC architectures," *IEEE Trans. Circuits Syst. I, Reg. Papers*, vol. 55, no. 6, pp. 1441–1454, Jul. 2008.

[33] M. Miyahara, Y. Asada, D. Paik, and A. Matsuzawa, "A low-noise self-calibrating dynamic comparator for high-speed ADCs," in *Proc. IEEE Asian Solid-State Circuits Conf.*, Nov. 2008, pp. 269–272.

[34] V. Giannini, P. Nuzzo, V. Chironi, A. Baschirotto, G. Van der Plas, and J. Craninckx, "An 820 μW 9 b 40 MS/s noise-tolerant dynamic-SAR ADC in 90 nm digital CMOS," in *IEEE Int. Solid-State Circuits Conf. (ISSCC) Dig. Tech. Papers*, Feb. 2008, pp. 238–610.

Jorge Lagos (Senior Member, IEEE) received the B.Sc. degree *(summa cum laude)* in electronics engineering from the Pontificia Universidad Católica del Perú (PUCP), Lima, Peru, in 2003, the M.Sc. degree *(cum laude)* in nanotechnologies for integrated systems from the Politecnico di Torino, Turin, Italy, the Institut Polytechnique de Grenoble, Grenoble, France, and the École Polytechnique Fédérale de Lausanne, Lausanne, Switzerland, in 2013, and the Ph.D. degree *(summa cum laude)* from Vrije Universiteit Brussel, Brussels, Belgium, in 2019, for his work on high-performance, power-efficient analog-to-digital converters, in collaboration with IMEC, Leuven, Belgium.

From 2004 to 2014, he occupied several Research Assistant positions with a focus on various topics. From 2004 to 2006, he was with PUCP, researching analog VLSI networks for channel decoding. From 2006 to 2011, he was with the Politecnico di Torino, working on chip-level electromagnetic compatibility and system-on-chip functional test. From 2012 to 2014, he was with the Fraunhofer Institute for Integrated Circuits, Erlangen, Germany, focusing on front-end design for MEMS sensors. In 2018, he joined IMEC, where he is currently a Senior Researcher in analog and mixed-signal IC design.

Dr. Lagos was a co-recipient of the 2019 International Solid-State Circuits Conference (ISSCC) Lewis Winner Award for outstanding paper.

Nereo Markulić (Member, IEEE) received the M.Sc. degree in electrical engineering from the University of Zagreb, Zagreb, Croatia, in 2012, and the Ph.D. degree *(summa cum laude)* from Vrije Universiteit Brussel, Brussels, Belgium, in 2018. His Ph.D. work was in collaboration with IMEC, Leuven, Belgium, on digital subsampling phase-locked loops (PLLs) and polar transmitters.

He is currently a Research Scientist at IMEC, working on RF and mixed-signal circuits for radar applications and next-generation connectivity. He has authored or coauthored publications and patents on PLLs and analog-to-digital converters, and a book on frequency synthesis.

Dr. Markulić serves on the Technical Program Committee of the IEEE Very Large Scale Integration (VLSI) Circuits Symposium. He was a co-recipient of the International Solid-State Circuits Conference (ISSCC) 2019 Lewis Winner Award for outstanding paper.

Benjamin Hershberg (Member, IEEE) received the H.B.S. degrees in electrical engineering and computer engineering and the Ph.D. degree in electrical engineering from Oregon State University, Corvallis, OR, USA, in 2006, and 2012, respectively, for his work in scalable, low-power switched-capacitor amplification solutions, inventing the techniques of Ring Amplification and Split-CLS.

From 2013 to 2021, he was a Principal Member of Technical Staff at the Interuniversity Microelectronics Center (imec), Leuven, Belgium, conducting research on topics encompassing the full receiver chain from RF frontends to ADCs. He currently works as an Independent Researcher and a Consultant with a focus on both integrated circuits and algorithms for machine learning.

Davide Dermit (Member, IEEE) received the B.S., M.S., and Ph.D. degrees in electrical engineering from the University of Modena and Reggio Emilia, Modena, Italy, in 2005, 2007, and 2011, respectively.

In 2008, he was an Internship Student with Entropic Communications, Sophia-Antipolis, Nice, France, working on high-speed digital PLL frequency synthesizers in 65-nm CMOS for cable-TV. From 2010 to 2015, he was an Analog and RF IC Designer with STMicroelectronics, Grenoble, France, working on I^{2}C shifters in 600-nm BCD for the HDMI standard and integrated 10–28-GHz receivers in 28–14-nm CMOS for multi-standard PHY and SerDes. From 2015 to 2021, he was an Analog and RF IC Designer with IMEC, Leuven, Belgium, working on Cartesian digital RF modulators in 28-nm CMOS for software defined radios and high-speed ADCs in 16-nm FinFET. In 2021, he joined arQana Technologies, Leuven, where he is currently working as a Principal Analog IC Designer on the development of beamforming ICs.

Dr. Dermit was a co-recipient of the 2019 Lewis Award for outstanding paper at the 2019 International Solid-State Circuits Conference (ISSCC).

Mithlesh Shrivas (Member, IEEE) received the B.Tech. and M.Tech. degrees in microelectronics from IIT Bombay, Mumbai, India, in 2004.

He joined Motorola, Noida, India, in 2004, and later Freescale Semiconductor, Noida, where he focused on the design of voltage regulators and ADCs. In 2011, he joined Intel Technology, Mumbai, where he developed voltage regulators in FinFET technologies. In 2014, he joined Samsung Electronics, Suwon, South Korea, where he worked in analog front-end design for smartphones. Since 2016, he has been a Research and Development Engineer with IMEC, Leuven, Belgium, where he focuses on the design of ADCs and RF baseband circuits.

Ewout Martens (Member, IEEE) received the M.Sc. degree in electronic engineering and the Ph.D. degree *(summa cum laude)* from the Katholieke Universiteit Leuven (KU Leuven), Leuven, Belgium, in 2001 and 2007, respectively, for research on modeling techniques for delta-sigma modulators and RF front-ends.

From 2007 to 2010, he worked in a spin-off company of KU Leuven as the Chief Scientist focused on analog design automation. In 2010, he joined IMEC, Leuven, as a Researcher for WLAN transceivers, where he is currently working as a Principal Member of Technical Staff within IMEC's Advanced RF Department. His research interests and works are related to the development of innovative architectures for RF receiver front-ends, transceiver building blocks like PLL, filters and LNA, and ADCs for various applications, including image sensors, wireless and wireline receivers.

Dr. Martens has served as a Technical Program Committee Member for the Symposium on Very Large Scale Integration (VLSI) Circuits from 2017 to 2020.

Jan Craninckx (Fellow, IEEE) received the M.S. and Ph.D. *(summa cum laude)* degrees in microelectronics from the ESAT-MICAS Laboratories, KU Leuven, Leuven, Belgium, in 1992 and 1997, respectively. His Ph.D. work was on the design of low-phase-noise CMOS integrated voltage-controlled oscillators (VCOs) and phase-locked loops (PLLs) for frequency synthesis.

From 1997 to 2002, he worked with Alcatel Microelectronics (later part of STMicroelectronics) as a Senior RF Engineer on the integration of RF transceivers for GSM, DECT, Bluetooth, and WLAN. In 2002, he joined IMEC, Leuven, as Principal Scientist, working on RF, analog, and mixed-signal circuit design. He is currently an IMEC Fellow. He has authored or coauthored more than 200 articles, book chapters, and patents. His research focuses on the design of RF transceiver front-ends in nanoscale CMOS, covering all aspects of RF, mmwave, analog, and data converter design.

Dr. Craninckx is/was a regular member of the Technical Program Committee for several Solid State Circuits Society (SSCS) conferences, was the Chair of the SSCS Benelux chapter from 2006 to 2011, SSCS Distinguished Lecturer from 2012 to 2013, and elected as a SSCS AdCom Member from 2017 to 2019. He currently serves as the RF Subcommittee Chair for the IEEE International Solid-State Circuits Conference. He was an Associate Editor (from 2009 to 2016) and the Editor-in-Chief (from 2016 to 2019) of the IEEE JOURNAL OF SOLID-STATE CIRCUITS.